JAAS

Laboratory X-ray Emission Spectrometer for Phosphorus Kα and Kβ Study of Air-Sensitive Samples

Journal:	*Journal of Analytical Atomic Spectrometry*
Manuscript ID	JA-ART-02-2023-000053.R1
Article Type:	Paper
Date Submitted by the Author:	04-Apr-2023
Complete List of Authors:	Abramson, Jared; University of Washington, Physics Holden, William; University of Washington, Physics; easyXAFS LLC Rivera-Maldonado, Ricardo; University of Washington, Chemistry Velian, Alexandra; University of Washington, Chemistry; Cossairt, Brandi M.; Univ Washington, ; University of Washington Seidler, Gerald; University of Washington, Physics

Laboratory X-ray Emission Spectrometer for Phosphorus Kα and Kβ Study of Air-Sensitive Samples

Jared E. Abramson[1*], William M. Holden[1,2,*], Ricardo A. Rivera-Maldonado[3], Alexandra Velian[3], Brandi M. Cossairt[3], Gerald T. Seidler[1,**]

[1] Physics Department, University of Washington, Seattle WA, USA 98195
[2] easyXAFS LLC, Renton WA, USA 98057
[3] Chemistry Department, University of Washington, Seattle WA, USA 98195

The analytical chemistry of phosphorus-containing materials is often impeded by the long measurement times and relatively large sample masses needed for ^{31}P NMR spectroscopy, by the scarcity and access limitations of synchrotron beamlines operating in the energy range of the P K-edge, by the challenges posed by species interconversion during liquid extraction, and by the considerable air-sensitivity typical of many phosphorus-containing materials and nanophases. To this end, we report the design and operation of a new laboratory-based spectrometer to simultaneously perform P Kα and Kβ X-ray emission spectroscopy (XES) while being housed in a research-grade controlled-atmosphere glovebox. Demonstration studies on nickel phosphide nanophases illustrate the importance of air-free XES and the value of simultaneous Kα and Kβ spectroscopy for identifying the P oxidation state and for investigating nanoscale influences on valence level electronic structure.

(*) co-first authors

(**) seidler@uw.edu

I. Introduction

Phosphorus is well known for its numerous biological functions and importance in nutrition [1-5], but is seeing strong contemporary interest for applications of black phosphorus and phosphorene [6-9] in addition to a steadily growing body of research on the catalytic properties of metal phosphides [8, 10-13]. Phosphorus-31 nuclear magnetic resonance (^{31}P NMR) spectroscopy has been a workhorse technique used, e.g., to study phosphorus chemistry in water and soil health [14-16] and also transition metal catalyst structure [17, 18]. However, ^{31}P NMR spectroscopy requires relatively large sample mass and suffers from long measurement times. An alternative, which is also element-specific and extremely local, is x-ray absorption spectroscopy (XAS). Synchrotron XAS strongly interrogates P electronic structure and environment but suffers from a poor fit with routine analytical application, the relatively few synchrotron beamlines operating in the energy range of the P K-edge, and the scarcity of such beamlines equipped with research-grade gloveboxes to support the extreme air-sensitivity of many P-rich compounds [19-21]. Synchrotron x-ray emission spectroscopy (XES) also informs P electronic structure and is performed at synchrotron beamlines to great effect [19, 21-24], but shares the above limitations of synchrotron XAS.

Recent work has, however, emphasized that some of the above issues surrounding access can be addressed with high-throughput laboratory XES for analytical application [25-30]. This includes laboratory-based study of the P Kα and Kβ XES of several systems [21, 29, 31, 32] with successful determination of oxidation state distribution, ligand identity, and bonding of various phosphorus compounds. Improved measurement times and smaller sample masses when compared to ^{31}P NMR spectroscopy have also been reported [29].

Building on these prior developments and addressing the added complexity of air-sensitivity of P-rich systems, we report here the design and commissioning of a new laboratory-based XES spectrometer that simultaneously measures the P Kα (core-to-core) and P Kβ (valence-to-core) XES while permanently installed in a research-grade controlled-atmosphere glovebox. This instrument uses the small footprint 'Dispersive Rowland Refocusing' (DRR) geometry[33] seen to have synchrotron-level performance across many studies despite the use of only a low-powered, low-brilliance conventional x-ray tube source [25, 33, 34]. We propose that the integration of

compact laboratory based XES instruments with controlled atmosphere gloveboxes holds high scientific and analytic potential, well beyond the present case of phosphorus.

II. Spectrometer Design

The general layout for each of the two tandem spectrometers follows the (DRR) geometry discussed in Holden, et al [33]. As shown in Fig. 1, a finite sized sample inside the Rowland circle is illuminated by an unfocused x-ray beam source having a 14 mm spot size at the sample location – the Rowland circle location is defined by the position and radius of curvature of the cylindrical analyzer optic. The optics and other key components of the two Rowland circles are shown in Fig. 2a and Fig. 2b. Computer aided design (CAD) renderings of the double spectrometer are shown in Fig. 2c and 2d. In Fig. 3, a photograph of the installed system and a CAD rendering showing the spectrometer and sample handling wheel are presented with components labeled.

The largest component is the controlled-atmosphere glovebox (M. Braun Complete Labstar Pro Glovebox System). This system has a hinged, removable front window to simplify spectrometer installation and maintenance. The spectrometer enclosure is a stainless-steel vacuum chamber (LACO Technologies) with inner dimensions 23 cm x 30 cm x 30 cm and 6.35-mm wall thickness, component 1 in Fig. 3. This enclosure acts as both a helium gas enclosure and as the primary radiation safety enclosure. There are multiple small KF-style flanges for helium gas handling and electrical feedthroughs. The sample is directly illuminated by x-rays from an air-cooled tube source (Varex VF-80 with a Pd anode) having a maximum electron beam power of 100W at 35kV accelerating potential (Spellman high-voltage supply, hardware-limited to 35 kV to simplify radiation shielding). This system provides a diverging, unfocused beam of combined bremsstrahlung and fluorescence radiation from a Pd anode. The x-ray tube is attached to the outside of a flange, Fig. 3 component 12 labeled ‘DRR flange’, which holds the other DRR elements and is fastened to the spectrometer enclosure.

Fluorescence from the sample can be diffracted by either of two 10-cm radius, cylindrically bent, Si (111) Johann analyzers (XRS Tech). These analyzers are positioned in separate DRR geometries of corresponding 10-cm diameter Rowland circles which are tilted and rotated with respect to each other, see Fig. 2 and component 7 in Fig. 3. The analyzers are 20 mm wide (in the Rowland planes) by 8 mm tall (perpendicular to Rowland planes)

and positioned at a 79.1° (2014.6eV) and 67.6° (2137.8eV) Bragg angle for phosphorus Kα and Kβ, respectively. Due to energy broadening caused by the relatively low Bragg angle for phosphorus Kβ, the edges of the Kβ crystal analyzer are masked with aluminum foil leaving only the central ~4 mm exposed. The masking is used to limit the energy deviation due to Johann error and is not needed for the Kα analyzer due to its more favorable Bragg angle; calculations related to this are shown in Fig. SI-3. The analyzers are held in a 3-D printed plastic mount that registers to the DRR flange by dowel pins to ensure correct positioning.

The diffracted fluorescence is detected by one of two energy-resolving x-ray cameras which have been previously reported [35], components 9 and 10 in Fig. 3. The x-ray camera detectors are mounted using 3-D printed plastic pieces registered against the DRR flange. The detectors are commercially available CMOS-based devices (IDS Imaging Development Systems Inc.) that have been modified by removing the image sensor glass cover to allow direct illumination of the CMOS sensor's active region by ~2 keV photons. The Kα detector is a UI-382LE camera with a Sony IMX 290 detector (1936 pixels x 1096 pixels) while the Kβ detector is a UI-3882LE camera with a Sony IMX 178 detector (3088 pixels x 2076 pixels). The 2.9-μm and 2.4- μm pixel sizes for the Sony IMX 290 and Sony IMX 178, respectively, correspond to energy broadenings of ~0.01 eV for Kα and ~0.02 for Kβ on our 10-cm Rowland circle. Given the small energy spacing between pixel-defined bins compared to the relevant core-hole broadening and minimum instrumental broadening due to the Si (111) Darwin width, we rebin all spectra on an 0.05 eV grid.

The sample mount assembly includes a 10-position sample wheel (component 11 in Fig. 3), attached by a small magnetic kinematic mount to a NEMA 11 bipolar stepper motor. Sample exchange is performed by first pulling the sample mount assembly away from the source via the linear slide rail and then detaching the sample wheel at the kinematic mount. This arrangement allows for easier installation and removal of samples inside of the glovebox, where manipulation is made more challenging by thick gloves.

III. Methods

III.A. Reference Sample Preparation

Nickel phosphide references were used to test the spectrometer and run the commissioning studies. Disodium hydrogen phosphate reference was used to set the energy scale by matching peaks to known energies [36], see Fig. SI-1. Pellets were made by pressing an approximately 1:1 mass ratio of commercial reference powders, Ni_2P (98%, Millipore-Sigma) or $Ni_3(PO_4)_2$ (98%, Alfa Aesar) or Na_2HPO_4 (98%, Millipore-Sigma), and BN powder (98%, Millipore-Sigma) into a 13-mm diameter die. These reference pellets were cut into approximately 10 mm x 5 mm x 1 mm sized pieces to fit in the spectrometer without collisions. Pellets were dried under vacuum at 80°C overnight prior to use in the glovebox.

III.B. Ni_2P Nanoparticle Synthesis

All glassware was dried at 160 °C overnight prior to use. All manipulations were performed using standard Schlenk techniques or inside a nitrogen atmosphere glovebox unless stated otherwise. nickel (II) chloride (98%, Millipore-Sigma) was dried at 100°C under vacuum overnight before being stored in a nitrogen glovebox for use. Oleylamine (90% Technical Grade, Millipore-Sigma), pentane, and toluene were dried over CaH_2, distilled, and stored over 4 Å sieves in a nitrogen glovebox. Tris(diethylamino)phosphine (97%, Millipore-Sigma), 2-propanol (99.5% Anhydrous, Millipore-Sigma), and acetonitrile (99.8% Anhydrous, Millipore-Sigma) was stored in a nitrogen glovebox and used as received.

To synthesize the Ni_2P nanoparticles in toluene, nickel (II) chloride (472 mg, 3.6 mmol) was quickly transferred from a glovebox to a 3-neck round bottom flask connected to a Schlenk line before the reaction vessel was purged and refilled with dry N_2 three times. Then oleylamine (24 mL) was quickly transferred from the glovebox to the reaction flask via syringe. The solution was heated to 120 °C using a thermal probe inserted into a thermal well in contact with solution and degassed for approximately one hour. Afterwards, heat was turned off, and the solution was placed under active N_2 flow and allowed to cool to approximately 70 °C.

Tris(diethylamino)phosphine (4.0 mL, 14 mmol) was then quickly transferred from the glovebox and injected into the reaction flask. The solution was heated to 250 °C and held for 1 hour prior to being cooled to near room temperature. Finally, the condenser columns and rubber septum were replaced with a glass stopper and

t-adapter while flowing an overpressure of N_2 before being transferred into the glovebox through 15 fast cycles of evacuation and refill in the glovebox antechamber.

The nanoparticle solution was purified by centrifugation at 7830 rpm for 15 min with a 1:10 volume ratio of solution to 2-propanol. This was followed three times by decanting the supernatant, dissolving the solid pellet in minimal pentane, again adding a 10x volume ratio of 2-propanol, and centrifuging at 7830 rpm for 15 min. Finally, the supernatant was decanted, minimal toluene was used to dissolve the solid pellet, a 1:4 volume ratio for solvent:antisolvent was used with acetonitrile as the antisolvent, and the solution was centrifuged at 7830 rpm for 15 min. The supernatant was decanted and the remaining solid was dissolved in pentane and dried under vacuum.

With the above synthesis completed, a concentrated solution of Ni_2P nanoparticles in toluene was drop cast on Si (100) wafers (Ted Pella). Seven replicate samples were made and mounted onto the sample wheel. The as-prepared samples are referred to as Ni_2P-0h (meaning zero hours of air exposure), and are subsequently renamed based on air exposure time as Ni_2P-1h, etc.

For the different air exposure times, nanoparticle samples were unmounted from the sample wheel and removed from the glovebox for needed incremental air exposures to achieve the desired cumulative air exposure. Then they were reloaded into the glovebox and remounted in the spectrometer.

III.C. Measurement protocols

All measurements were performed at ~100W x-ray tube power, i.e., at 2.8-mA tube current and 35-kV accelerating potential. The instrument is allowed to thermalize for at least half an hour at the desired power before data collection – no spectral drift is observed between chronologically early and late scans. Prior to data acquisition, the spectrometer enclosure is flushed with helium gas for about 15 minutes until the counts for a reference sample plateau.

To minimize potential errors from finite sample size, sample homogeneity, or analyzer irregularities, we follow the methods of Abramson, et al. [25]. This is done by taking short two-minute camera exposures at each position while stepping individual samples by ~0.44 mm through the illumination region and summing the

resulting spectra. This gives equal weight at all detected energies to all positions on the face of the sample regardless of size or concentration. Using this protocol, P Kα and Kβ spectra were collected as x-ray camera images for nanoparticle samples exposed to air for various amounts of time, and reference compounds. Data was taken twice at each position on seven replicate samples for a total collection time of ~80 minutes per replicate sample during which Kα and Kβ are collected simultaneously. This was repeated for each air exposure time.

Control software for the instrument is written in Python, and the user interface is presented in Jupyter. Users specify a sample map with each entry containing a name, sample wheel position, and integration time. Then, calling names given in the sample map, a list of scans is set up to run automatically with x-ray camera images saved for each scan.

The camera images for one sample are summed over the sample wheel movement to form a single image, Fig. 4 shows summed representative x-ray camera images for the dispersed fluorescence from a Ni_2P-0h nanoparticle. In this image the energy dispersive direction is horizontal, and the vertical direction shows the out of plane divergence. The curvature of the fluorescence on the camera face is due to the cylindrical analyzer geometry and is parameterized using a second order polynomial fit to the center-of-masses calculated for each row after Gaussian filtering. The coefficients for this polynomial are used to assign each pixel of the detector to an energy bin, and the intensities with each such label are summed to produce the spectrum (processing software courtesy of easyXAFS LLC [35]). The energy scale is then set by measurement of Na_2HPO_4, having $K\alpha_1$ and $K\beta_{1,3}$ energies at 2014.55 eV and 2137.80 eV, respectively, based on Petric et. al.[36].

The spectra of all seven replicate samples at each time point were summed. Kα spectra were background subtracted by a linear background calculated using the first and last 2 eV of the spectra, and then integral normalized. Kβ spectra were background subtracted by a linear background calculated using the first and last 5 eV of the measurement, and then normalized using the associated Kα integral to put them on an approximate mole-weighted scale.

III.D Analysis Techniques

Linear superposition fitting was performed in `Mathematica` for the Ni_2P nanoparticle Kα spectra, using the Ni_2P-Bulk and $Ni_3(PO_4)_2$ reference spectra as end points. The energy of the endpoint spectra was allowed to shift in order to accommodate the small differences in Kα energies known to occur within one, nominal, oxidation state [36]. These shifts averaged 0.013 eV for the phosphide reference and 0.10 eV for the phosphate reference.

III.E. Electronic Structure Calculation

The FEFF10 real-space multiple-scattering code [37, 38] was used to calculate the XES using self-consistent potentials (SCP), full-multiple-scattering (FMS), and Hedin-Lundqvist self-energy corrections. The use of FEFF10 for valence-to-core XES calculation has been discussed previously, such as in Mortensen, et al [39]. The cluster sizes used in the calculations were 6 Å for both the SCP and FMS calculations. For the bulk calculation, the structure was taken as the hexagonal crystal structure [40] with space group p-62m. The Kβ XES was then calculated for each of the two inequivalent sites in the unit cell and stoichiometrically averaged to obtain the total Kβ XES spectrum. To approximate the surface Kβ XES spectrum of the nanoparticle, a 9 Å cluster was cut from the bulk, and the spectra of all surface P atoms were averaged.

IV. Results and Discussion

To begin, we show in Fig. 5 a representative averaged sample fit of Ni_2P-24h, using a linear superposition fitting to phosphide (Ni_2P-Bulk) and phosphate ($Ni_3(PO_4)_2$) reference compound endpoints. In the top panel, the fit is done with no broadening of the two endpoint reference spectra, and the residual shows clear discrepancies indicating a weakness of the model. This isn't unexpected, as the nanophase materials have inhomogeneity from both their surface truncation (even if there are no surface adsorbates or other complications) and from the presence of an amorphous layer at the surface [41]. These effects are discussed further in the following paragraphs. Because of this inhomogeneity, we include 0.2 eV broadening of the reference spectra to allow for small differences in the Kα energies from slightly different local environments. The resulting fit, shown in the bottom

panel of Fig. 5, is much improved. Fits for the entire aging sequence are shown in Fig. SI-2. In general, we find a statistical error in the fraction phosphide of 0.01 or less from the standard error determined from the seven replicate samples at each time point, see Table SI-1 and Table SI-2 for replicate fraction phosphide, standard deviation, and standard error. We also estimate a systematic error of the fitting of ±0.02 due to uncertainties in the use of the broadened-fit model.

Next, in Fig. 6 we show P Kα data for Ni_2P nanoparticles that have been exposed to air for differing lengths of time, the phosphide reference, Ni_2P-Bulk, and the phosphate reference, $Ni_3(PO_4)_2$. The reference spectra show the typical Kα line shape, i.e., two peaks ($K\alpha_1$ and $K\alpha_2$) with a roughly 2:1 peak intensity ratio and a small trough in between. Based on fits to two Voight profiles that incorporate known corehole lifetimes for the P 2p states, we estimate an energy resolution of ~0.3 eV for the Kα spectrometer; see Fig. SI-4. for example, when comparing our Na_2HPO_4 spectra, used for energy calibration and shown in SI-1, to synchrotron spectra from Petric et. al.[36]. Additionally, the reference spectra show the expected trend in energy shift with oxidation state.

The air-exposed, replicate-averaged Ni_2P nanoparticle spectra, to varying degrees, no longer show just two distinct $K\alpha_1/K\alpha_2$ peaks, indicating a mixed P oxidation state. The increase in intensity at 2014.55 eV paired with the decrease in intensity at 2013.80 eV (the two gray energy bands in Fig. 6) indicates a shift to a larger percentage of highly oxidized P upon increased air exposure. Fig. 6b shows the Ni_2P nanoparticle spectra have an approximate isosbestic point suggesting that the transition in P oxidation is a simple two-phase mixture. Given this, linear combination fitting of the Ni_2P nanoparticle spectra was performed to obtain a value for the fraction of P which has not been oxidized, listed in Fig. 6a as fraction phosphide.

In Fig. 7 we show Kβ spectra for the Ni_2P nanoparticles and references; again, this is collected simultaneously with the Kα results shown in Fig. 6. The Kβ reference spectra show all the expected features with high energy resolution, main $K\beta_{1,3}$ peak, oxygen ligand Kβ' peak for $Ni_3(PO_4)_2$, and Kβ'' side peak for Ni_2P-Bulk. The lack of features with known lifetimes makes it difficult to estimate the energy resolution of the Kβ spectrometer, but the good performance certainly indicates energy resolution safely better than 0.8 eV. These reference Kβ spectra agree with previous phosphate and phosphide results [29, 36, 42]. The Ni_2P nanophase Kβ

spectra, interestingly, show both similarities and differences with respect to the reference compounds. This is particularly notable when comparing the Ni_2P-Bulk reference to Ni_2P-0h nanoparticle sample -- the Ni_2P-0h nanoparticle sample contains only about 4% phosphate from the P Kα fitting and, therefore, our initial expectation was that the Kβ spectra of the nanophase would agree well with that of the bulk Ni_2P.

The main difference is the spectral line shape of the main $K\beta_{1,3}$ peak (~2137.80 eV), both in terms of its greater width and the decreased prominence of the Kβ'' side peak (~2142.00 eV). It is important to remember, however, that the nanoparticles have a mean diameter of only 5 nm and, further, that transmission electron microscopy (TEM) typically shows a disordered Ni- and P- containing layer at the surface. Comparing average sizes of nanoparticles obtained by analyzing TEM images (~5 nm in diameter) and average crystallite domain sizes obtained by applying the Scherrer equation to peaks in the diffractogram (~4 nm in diameter) demonstrates that the surface layer is approximately 0.5 nm. Surface amorphization is seen in other studies as well [43-46], including one which estimated the disordered surface layer thickness of Ni_2P nanoparticles to be between 0.55 nm and 0.75 nm depending on surface facet terminations [41]. While it is not possible to model this disordered phase without additional information about its composition, the general effect of the nanoparticle surface, compared to bulk, on electronic structure can be modeled. In Fig. 8 we show the predicted bulk and near-surface contributions for an idealized crystalline Ni_2P nanoparticle. The general character of the deviation between the bulk Ni_2P and the native nanophase Ni2P-0h is in reasonable agreement between data and theory – the Kβ'' side peak shifts to lower energy and the main $K\beta_{1,3}$ peak broadens.

Hence, while we can perform a simple linear superposition analysis of the Kα spectra to extract an estimate of P oxidation, no similar analysis is possible with the Kβ spectra, apparently due to electronic and structural differences near the surface of the nanoparticles. That being said, the Kβ data does show an increased presence of P-O bonds (i.e. higher oxidation state P) with longer air exposure via the increasing strength of the oxygen ligand peak, Kβ' at ~2124 eV.

The increased air exposure of the Ni_2P nanoparticle samples show a consistent increase in phosphate character across both Kα and Kβ spectra. In Fig. 9. We show the phosphide fraction, derived from fitting the Kα spectra to the references (as above) and a scaled representation of the integral of the oxygen ligand peak in the Kβ

spectra, both plotted against the square root of air exposure time. Although the intensity of the ligand integral should be roughly proportional to the occurrence of P-O bonding, the absence of a valid fully-oxidized reference compound because of nanoscale effects discussed above, along with the effects of extreme sensitivity to oxygen ligand 2s energy and bond length [47], makes it impossible to assign a phosphide fraction metric to the ligand peak integral intensity on its own basis. Hence, the ligand integral results are scaled by the Kα-derived phosphide fractions at the 0 h and 336 h extrema -- the resulting general agreement is clear. The roughly linear trend as a function of the square root of air exposure time hints at a diffusion-limited model of P oxidation in the Ni_2P nanoparticles.

V. Conclusions

We report the design and performance of a new x-ray emission spectrometer that simultaneously measures P Kα and Kβ XES while being housed in a research grade, controlled atmosphere glovebox. A commissioning study of the gradual oxidation of Ni_2P nanoparticles due to air exposure showed excellent energy resolution and short acquisition times for both P Kα and Kβ XES. This system is housed in a shared user facility and provided with a user-friendly scripting interface. We anticipate that this system will see a wide range of future applications on air-sensitive P-rich materials while also serving as a proof-of-principle for future laboratory XES systems in research-grade gloveboxes.

Acknowledgements

The research was funded by the University of Washington Molecular Engineering Materials Center under U.S. National Science Foundation award DMR-1719797 and also by the U.S. National Science Foundation under award CHE-1904437. Jared Abramson acknowledges support from the University of Washington Clean Energy Institute and Rivera-Maldonado would like to thank the ARCS Foundation for additional funding.

REFERENCES

1. Alori, E.T., B.R. Glick, and O.O. Babalola, *Microbial Phosphorus Solubilization and Its Potential for Use in Sustainable Agriculture.* Frontiers in Microbiology, 2017. **8**. 971
2. Lopez-Arredondo, D.L., et al., *Phosphate Nutrition: Improving Low-Phosphate Tolerance in Crops*, in *Annual Review of Plant Biology, Vol 65*, S.S. Merchant, Editor. 2014. p. 95-123.
3. Menezes-Blackburn, D., et al., *Opportunities for mobilizing recalcitrant phosphorus from agricultural soils: a review.* Plant and Soil, 2018. **427**(1-2): p. 5-16
4. Veneklaas, E.J., et al., *Opportunities for improving phosphorus-use efficiency in crop plants.* New Phytologist, 2012. **195**(2): p. 306-320
5. Yaakob, M.A., et al., *Influence of Nitrogen and Phosphorus on Microalgal Growth, Biomass, Lipid, and Fatty Acid Production: An Overview.* Cells, 2021. **10**(2). 393
6. Li, B.S., et al., *Black Phosphorus, a Rising Star 2D Nanomaterial in the Post-Graphene Era: Synthesis, Properties, Modifications, and Photocatalysis Applications.* Small, 2019. **15**(8). 1804565
7. Liu, H., et al., *Semiconducting black phosphorus: synthesis, transport properties and electronic applications.* Chemical Society Reviews, 2015. **44**(9): p. 2732-2743
8. Pang, J.B., et al., *Applications of Phosphorene and Black Phosphorus in Energy Conversion and Storage Devices.* Advanced Energy Materials, 2018. **8**(8). 1702093
9. Xu, Y.J., et al., *Recent progress in black phosphorus and black-phosphorus-analogue materials: properties, synthesis and applications.* Nanoscale, 2019. **11**(31): p. 14491-14527
10. Liu, W.L., H.Q. Zhi, and X.B. Yu, *Recent progress in phosphorus based anode materials for lithium/sodium ion batteries.* Energy Storage Materials, 2019. **16**: p. 290-322
11. Rahman, M.Z., et al., *2D phosphorene as a water splitting photocatalyst: fundamentals to applications.* Energy & Environmental Science, 2016. **9**(3): p. 709-728
12. Shi, R., et al., *Black/red phosphorus quantum dots for photocatalytic water splitting: from a type I heterostructure to a Z-scheme system.* Chemical Communications, 2019. **55**(83): p. 12531-12534
13. Wu, Y., et al., *The Promise and Challenge of Phosphorus-Based Composites as Anode Materials for Potassium-Ion Batteries.* Advanced Materials, 2019. **31**(50). 1901414
14. Garcia-Oliva, F., et al., *Severe wildfire hinders renewal of soil P pools by thermal mineralization of organic P in forest soil: Analysis by sequential extraction and P-31 NMR spectroscopy.* Geoderma, 2018. **309**: p. 32-40
15. Huang, R.X. and Y.Z. Tang, *Speciation Dynamics of Phosphorus during (Hydro)Thermal Treatments of Sewage Sludge.* Environmental Science & Technology, 2015. **49**(24): p. 14466-14474
16. Schmieder, F., et al., *Phosphorus speciation in a long-term manure-amended soil profile - Evidence from wet chemical extraction, P-31-NMR and P K-edge XANES spectroscopy.* Geoderma, 2018. **322**: p. 19-27
17. Andrews, P., et al., *Highly active homogeneous nickel catalysts for alkene dimerisation: crystal strucure [Ni(η^3-C_3H_5)(PPh_3)Br] and in situ characterisation of $AlEt_3$-activated [Ni(η^3-C_3H_5)(PPh_3)Br] by nuclear magnetic resonance and extended X-ray absorption fine structure spectroscopy.* Journal of the Chemical Society-Dalton Transactions, 1994(9): p. 1337-1347
18. Liu, C., et al., *Topological construction of phosphorus and carbon composite and its application in energy storage.* Energy Storage Materials, 2019. **20**: p. 343-372
19. Sahkouri, M., et al., *Glovebox-integrated XES and XAS station for in situ studies in tender x-ray region.* Electronic Structure, 2020. **2**(4). 047001
20. Scheinost, A.C., et al., *ROBL-II at ESRF: a synchrotron toolbox for actinide research.* Journal of Synchrotron Radiation, 2021. **28**: p. 333-349
21. Li, M.S., et al., *New Insights into the High-Performance Black Phosphorus Anode for Lithium-Ion Batteries.* Advanced Materials, 2021. **33**(35). 2101259

22. Petric, M., et al., *Electronic Structure of Third-Row Elements in Different Local Symmetries Studied by Valence-to-Core X-ray Emission Spectroscopy.* Inorganic Chemistry, 2016. **55**(11): p. 5328-5336
23. Petric, M. and M. Kavčič, *Chemical speciation via X-ray emission spectroscopy in the tender X-ray range.* Journal of Analytical Atomic Spectrometry, 2016. **31**(2): p. 450-457
24. Mathe, Z., et al., *Phosphorus Kβ X-ray emission spectroscopy detects non-covalent interactions of phosphate biomolecules in situ.* Chemical Science, 2021. **12**(22): p. 7888-7901
25. Abramson, J.E., et al., *An exploration of benchtop X-ray emission spectroscopy for precise characterization of the sulfur redox state in cementitious materials.* X-Ray Spectrometry, 2022. **51**(2): p. 151-162
26. Holden, W.M., G.T. Seidler, and S. Cheah, *Sulfur Speciation in Biochars by Very High Resolution Benchtop K alpha X-ray Emission Spectroscopy.* Journal of Physical Chemistry A, 2018. **122**(23): p. 5153-5161
27. Jahrman, E.P., G.T. Seidler, and J.R. Sieber, *Determination of Hexavalent Chromium Fractions in Plastics Using Laboratory-Based, High-Resolution X-ray Emission Spectroscopy.* Analytical Chemistry, 2018. **90**(11): p. 6587-6593
28. Malzer, W., et al., *A laboratory spectrometer for high throughput X-ray emission spectroscopy in catalysis research.* Review of Scientific Instruments, 2018. **89**(11): p. 113111
29. Stein, J.L., et al., *Probing Surface Defects of InP Quantum Dots Using Phosphorus K alpha and K beta X-ray Emission Spectroscopy.* Chemistry of Materials, 2018. **30**(18): p. 6377-6388
30. Zimmermann, P., et al., *Modern X-ray spectroscopy: XAS and XES in the laboratory.* Coordination Chemistry Reviews, 2020. **423**. 213466
31. Mitra, K.L.W., et al., *Surface Functionalization of Black Phosphorus with Nitrenes: Identification of P=N Bonds by Using Isotopic Labeling.* Angewandte Chemie-International Edition, 2021. **60**(16): p. 9127-9134
32. Tetef, S., et al., *Informed Chemical Classification of Organophosphorus Compounds via Unsupervised Machine Learning of X-ray Absorption Spectroscopy and X-ray Emission Spectroscopy.* The Journal of Physical Chemistry A, 2022. **126**(29): p. 4862-4872
33. Holden, W.M., et al., *A compact dispersive refocusing Rowland circle X-ray emission spectrometer for laboratory, synchrotron, and XFEL applications.* Review of Scientific Instruments, 2017. **88**(7): p. 073904. 073904
34. Holden, W.M., et al., *Probing Sulfur Chemical and Electronic Structure with Experimental Observation and Quantitative Theoretical Prediction of K alpha and Valence-to-Core K beta X-ray Emission Spectroscopy.* Journal of Physical Chemistry A, 2020. **124**(26): p. 5415-5434
35. Holden, W.M., et al., *A color x-ray camera for 2-6 keV using a mass produced back illuminated complementary metal oxide semiconductor sensor.* Review of Scientific Instruments, 2018. **89**(9): p. 093111. 093111
36. Petric, M., et al., *Chemical State Analysis of Phosphorus Performed by X-ray Emission Spectroscopy.* Analytical Chemistry, 2015. **87**(11): p. 5632-5639
37. Kas, J.J., et al., *Advanced calculations of X-ray spectroscopies with FEFF10 and Corvus.* Journal of Synchrotron Radiation, 2021. **28**: p. 1801-1810
38. Rehr, J.J. and R.C. Albers, *Theoretical approaches to x-ray absorption fine structure.* Reviews of Modern Physics, 2000. **72**(3): p. 621-654
39. Mortensen, D.R., et al., *Benchmark results and theoretical treatments for valence-to-core x-ray emission spectroscopy in transition metal compounds.* Physical Review B, 2017. **96**(12). 125136
40. Larsson, E., *An X-ray investigation of Ni-P system and crystal structures of NiP and NiP_2.* Arkiv for Kemi, 1965. **23**(3-4): p. 335-&
41. Papawassiliou, W., et al., *Crystal and electronic facet analysis of ultrafine Ni2P particles by solid-state NMR nanocrystallography.* Nature Communications, 2021. **12**(1): p. 4334
42. Sugiura, C., *X-Ray Emission Spectra and Electronic Structures of Red Phosphorus, 3d Transition-Metal Phosphides and III–V Compounds.* Journal of the Physical Society of Japan, 1995. **64**(7): p. 2510-2523

43. Wang, J., A.C. Johnston-Peck, and J.B. Tracy, *Nickel Phosphide Nanoparticles with Hollow, Solid, and Amorphous Structures.* Chemistry of Materials, 2009. **21**(19): p. 4462-4467
44. Moreau, L.M., et al., *Defining Crystalline/Amorphous Phases of Nanoparticles through X-ray Absorption Spectroscopy and X-ray Diffraction: The Case of Nickel Phosphide.* Chemistry of Materials, 2013. **25**(12): p. 2394-2403
45. Mundy, M.E., et al., *Aminophosphines as Versatile Precursors for the Synthesis of Metal Phosphide Nanocrystals.* Chemistry of Materials, 2018. **30**(15): p. 5373-5379
46. Murphy, I.A., et al., *Covalent Functionalization of Nickel Phosphide Nanocrystals with Aryl-Diazonium Salts.* Chemistry of Materials, 2021. **33**(24): p. 9652-9665
47. MacMillan, S.N., et al., *Ligand-Sensitive But Not Ligand-Diagnostic: Evaluating Cr Valence-to-Core X-ray Emission Spectroscopy as a Probe of Inner-Sphere Coordination.* Inorganic Chemistry, 2015. **54**(1): p. 205-214

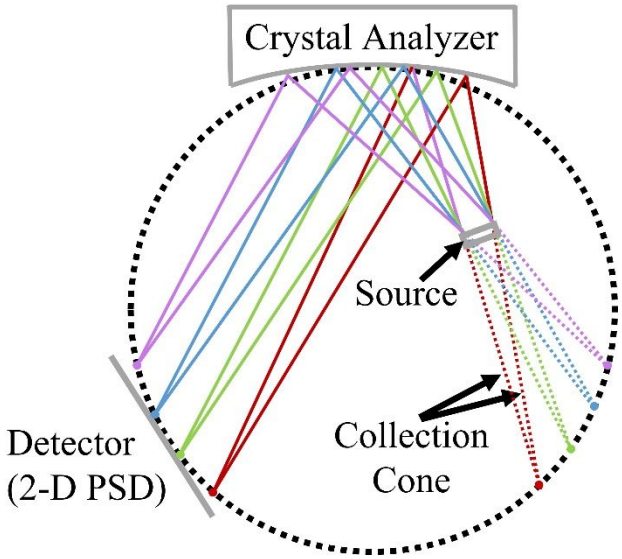

Figure 1. Dispersive Rowland Refocusing (DRR) geometry with a large source off-circle. The geometry has a bent crystal analyzer at the top of the circle, a position sensitive detector on the lower left of the circle, and virtual sources on a lower right arc each with an associated collection cone. The sample ('source' in this context) is illuminated by an X-ray source perpendicular to the circle. Note the spectral refocusing onto the detector arc and x-ray camera face.

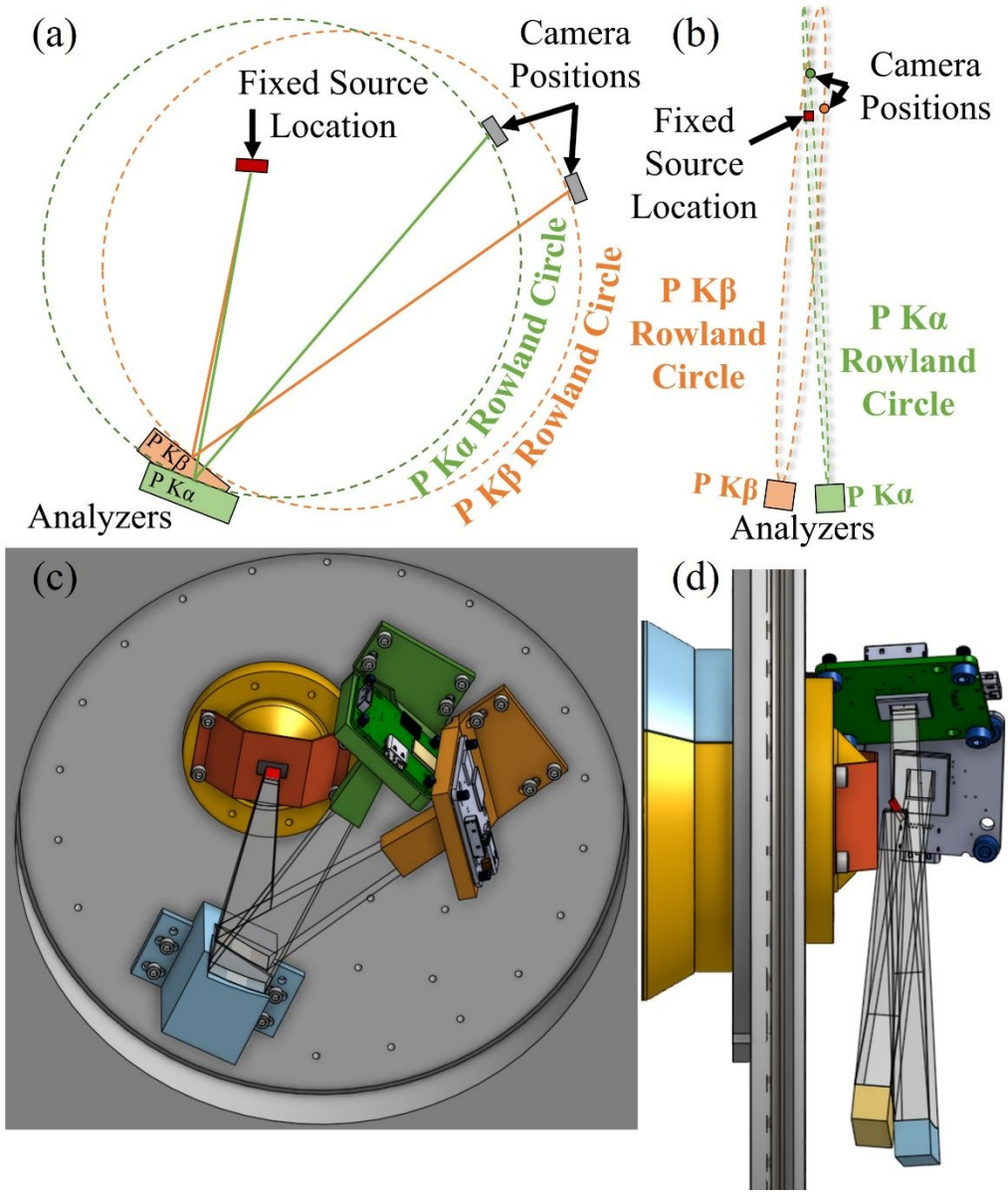

Figure 2. (a) Front and (b) side view illustration of the double Rowland circle geometry, with accompanying CAD rendering also from (c) front and (d) side views. The P Kα and P Kβ Rowland circles share the same source location but are translated and tilted out of plane to allow clearance for a 79.1° (2014.6eV) and 67.6° (2137.8eV) Bragg angle respectively. The mount of the crystal analyzers is omitted from Fig. 2d so that the analyzer orientations are more readily apparent and the stray scatter shields for the cameras are similarly omitted in that figure panel.

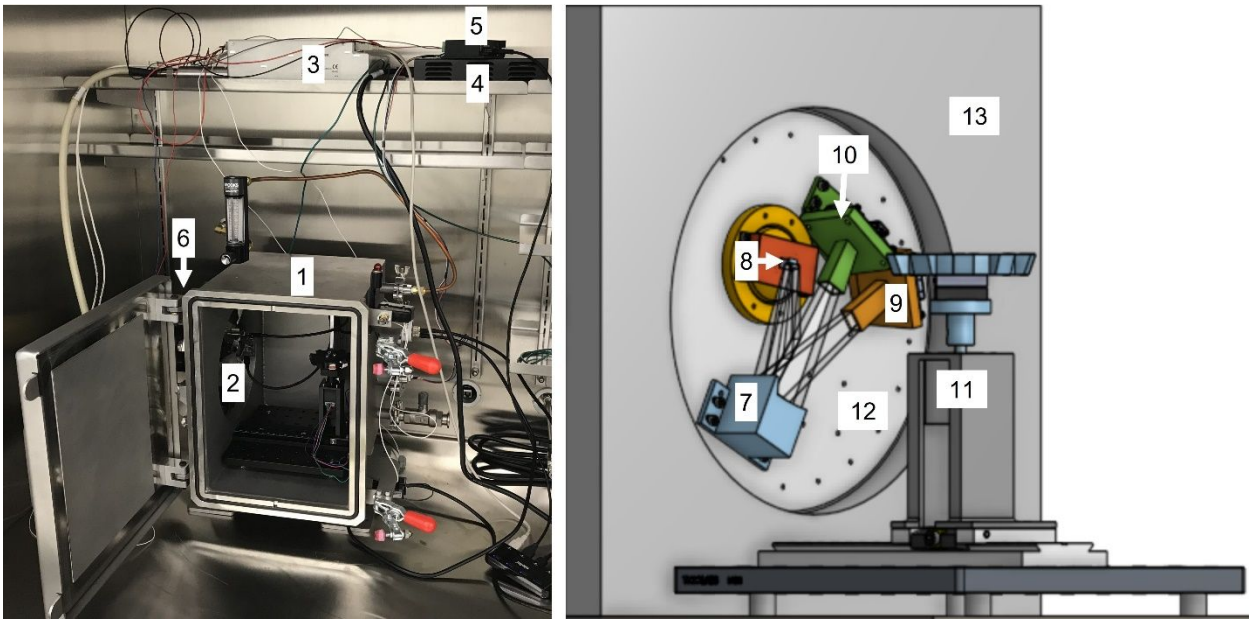

Figure 3. Photograph of the spectrometer placed in a glovebox with accompanying CAD rendering of the spectrometer components. Components include: (1) Helium enclosure; (2) spectrometer components (see 7-13 for more detail); (3) High voltage supply; (4) Power source; (5) Motor controller; (6) X-ray tube (hidden behind door in photo); (7) Two Si (111) crystal analyzers and mount; (8) Sample location; (9) P Kα x-ray camera and housing; (10) P Kβ x-ray camera and housing; (11) Sample mount containing sample wheel, magnetic mount and stepper motor; (12) DRR flange; (13) Helium enclosure wall. For clarity of presentation, the front window of the glovebox was removed for the photograph and the sample wheel assembly has been pulled back from the measurement position in both the photograph and the CAD.

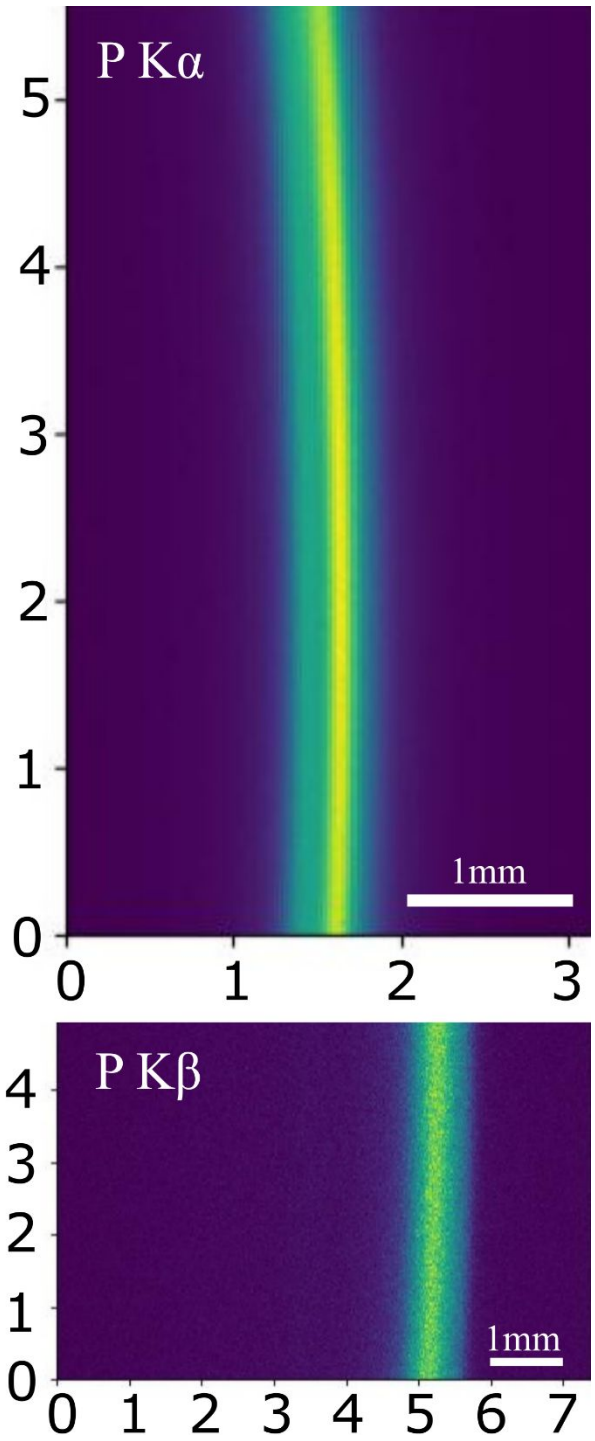

Figure 4. X-ray camera images of the dispersed fluorescence from a Ni_2P-0h nanoparticle sample: P Kα (above) and Kβ (below). The dispersive direction is horizontal, lower to higher energy moving left to right. The vertical direction shows the out of plane dimension, where minor curvature is observed from geometric effects causing photons to be bent towards lower energy. The pixel intensity shown is from the CMOS sensor's analog to digital converter and is different from photon count because of sensor gain.

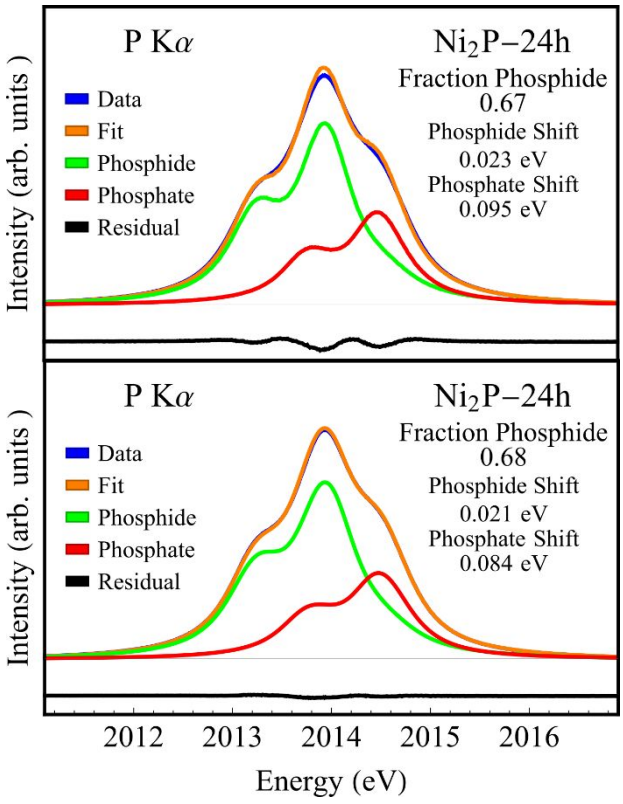

Figure 5. Linear superposition fit of the P Kα spectrum for an aged Ni2P nanophase sample to the phosphide (Ni_2P-Bulk) and phosphate ($Ni_3(PO_4)_2$) references. (a) Fits using the reference spectra as directly measured. (b) Fits after the reference spectra have been broadened by 0.2eV to compensate for a range of local environments, see the text for discussion. A compendium of fits for all air exposure times, using both broadened and unbroadened references, is presented in Fig. SI-2.

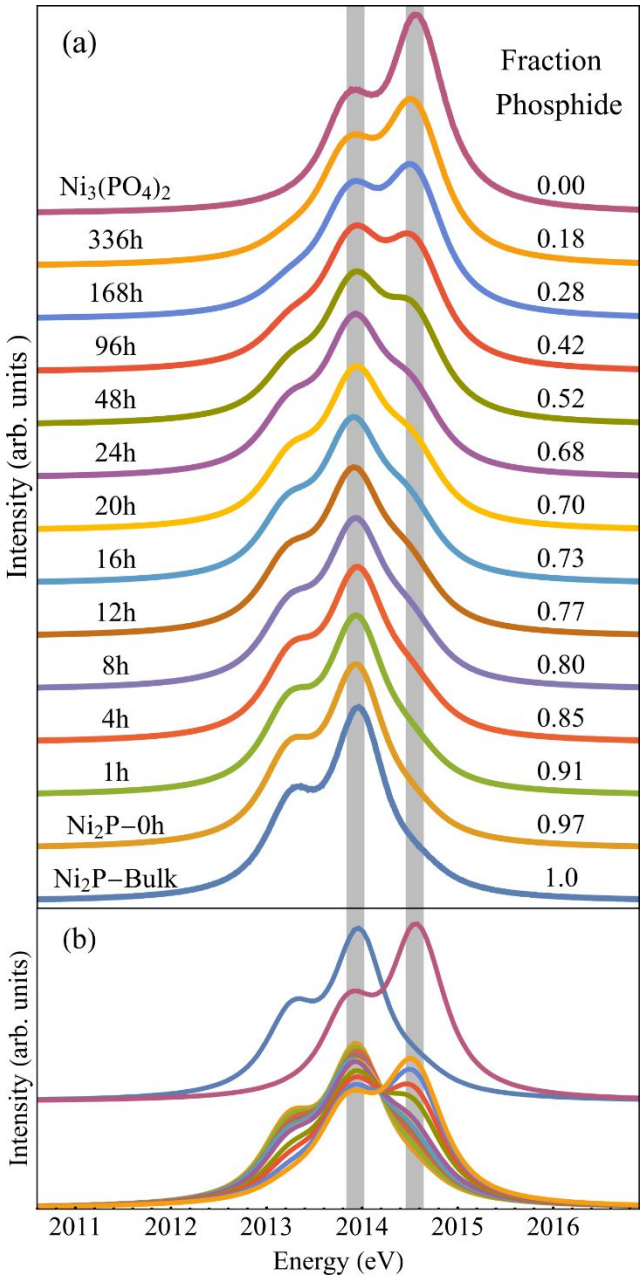

Figure 6. P Kα data for the Ni_2P-0h nanoparticles exposed to air for differing lengths of time, and two reference samples, Ni_2P-Bulk and $Ni_3(PO_4)_2$. Typical total measurement times for the ensemble of seven nanophase samples (averaged to give the results shown) is 9 hours, ~80 minutes per sample. Panel (a) shows the spectra offset with vertical guides, shaded bands, for the $K\alpha_1$ peaks of the phosphide and phosphate reference compounds. Panel (b) shows the same spectra overlayed. Note the apparent isosbestic point ~2014.25 eV, supporting the use of a simple two-phase decomposition onto reference compounds.

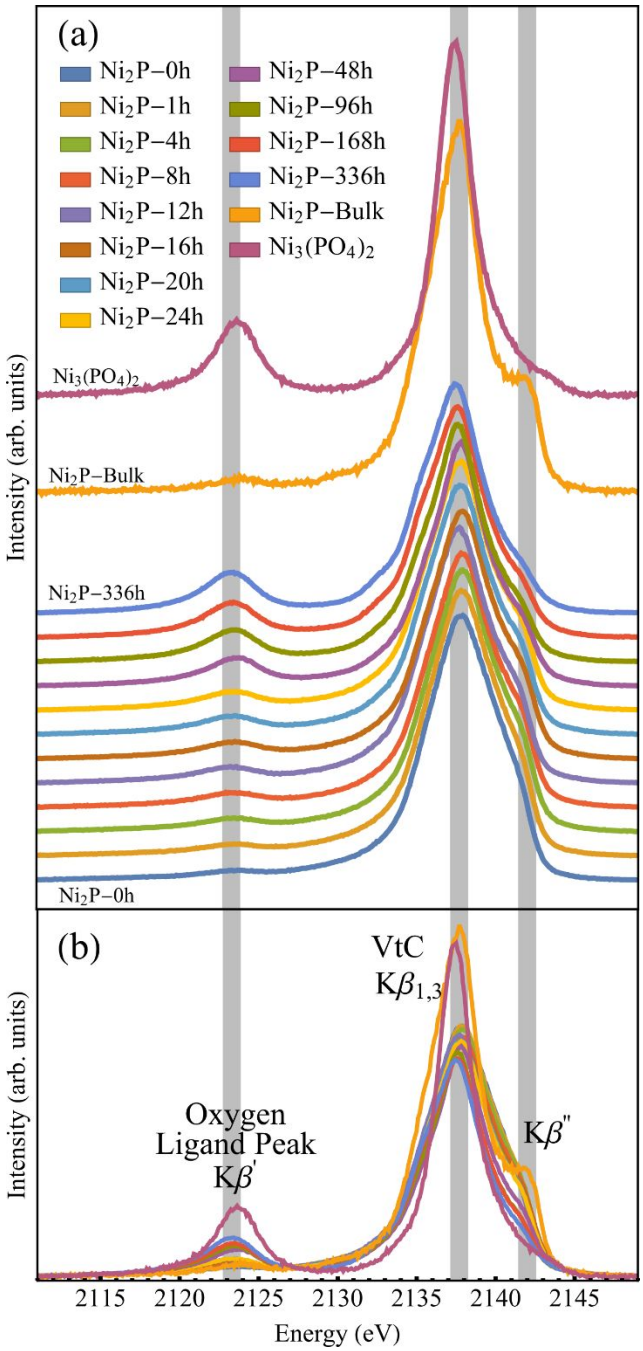

Figure 7. P Kβ spectra for the aging sequence of Ni_2P nanoparticles and the two reference samples, Ni_2P-Bulk and $Ni_3(PO_4)_2$. Note that as the air exposure time of the samples increases, there is a subtle shift in the main $K\beta_{1,3}$ peak and satellite $K\beta''$ peak, in addition to a steady increase in the intensity of the oxygen ligand peak.

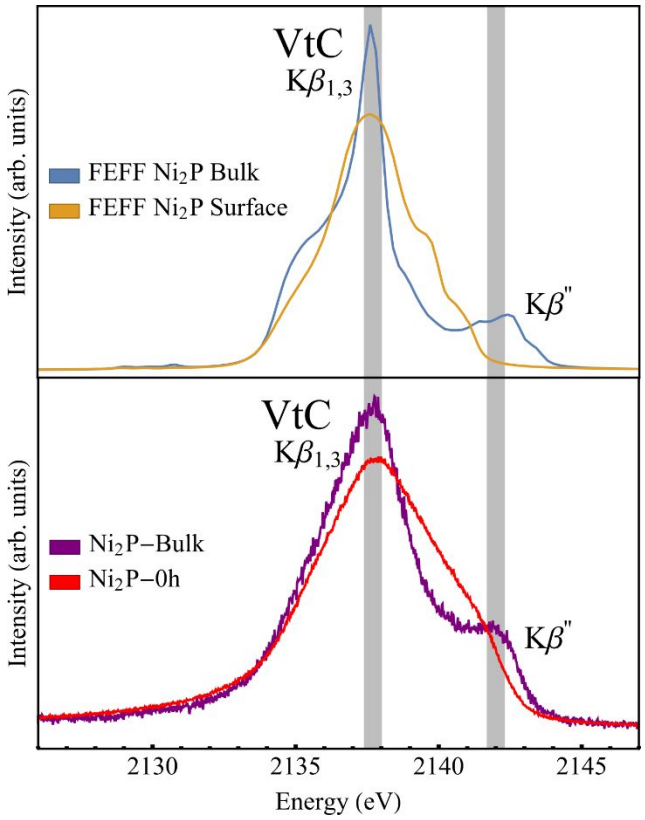

Figure 8. FEFF calculations for Ni_2P Bulk and Ni_2P Surface materials shown with data for Ni_2P-Bulk and Ni_2P nanoparticles, Ni_2P-0h. The differences between the bulk and surface theoretical spectra are in qualitative agreement with the deviations between the (macroscopic) crystalline Ni_2P-Bulk reference and the Ni_2P-0h spectra.

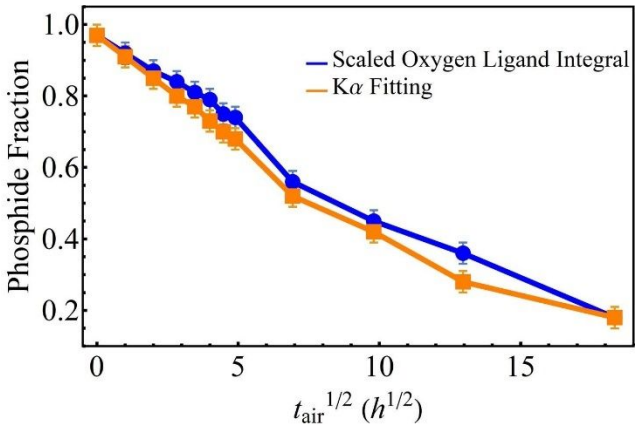

Figure 9. The phosphide fraction extracted from fits to Kα and from scaling of the oxygen ligand integral in Kβ (see the text), as a function of the square root of air exposure time, $t_{air}^{1/2}$. Both plots show a negative trend with increasing air exposure in rough agreement with a diffusion-limited model of oxidation.